Springer

Acta Mechanica Sinica

CrossMark click for updates

• RESEARCH PAPER •

Acta Mech. Sin., Vol. 39, 723169 (2023)
https://doi.org/10.1007/s10409-023-23169-x

Design of compliant mechanisms for origami metamaterials

Yasuhiro Miyazawa[1], Hiromi Yasuda[2], and Jinkyu Yang[1,3*]

[1] *Department of Aeronautics and Astronautics, University of Washington, Seattle, Washington 98195, USA;*
[2] *Aviation Technology Directorate, Japan Aerospace Exploration Agency, Mitaka, Tokyo 1810015, Japan;*
[3] *Department of Mechanical Engineering, Seoul National University, 1 Gwanak-ro, Gwanak-gu, Seoul 08826, Republic of Korea*

Received April 9, 2023; accepted April 28, 2023; published online xx xx, 2023

As an art of paper folding, origami has been widely explored by artists for centuries. Only in recent decades has it gained attention from mathematicians and engineers for its complex geometry and rich mechanical properties. The surge of origami-inspired metamaterials has opened a new window for designing materials and structures. Typically, to build origami structures, a sheet of material is folded according to the creaselines that are marked with compliant mechanisms. However, despite their importance in origami fabrication, such compliant mechanisms have been relatively unexplored in the setting of origami metamaterials. In this study, we explore the relationship between the design parameters of compliant mechanisms and origami mechanical properties. In particular, we employ single hinge crease and Kresling origami, representative examples of rigid and non-rigid origami units, fabricated using a double-stitch perforation compliant mechanism design. We conduct axial compression tests using different crease parameters and fit the result into the bar-hinge origami model consisting of axial and torsional springs. We extract the relationship between the spring coefficients and crease parameters using Gaussian process regression. Our result shows that the change in the crease parameter contributes significantly to each spring element in a very different manner, which suggests the fine tunability of the compliant mechanisms depending on the mode of deformation. In particular, the spring stiffness varies with the crease parameter differently for rigid and non-rigid origami, even when the same crease parameter is tuned. Furthermore, we report that the qualitative static response of the Kresling origami can be tuned between monostable and bistable, or linear and nonlinear, by only changing the crease parameter while keeping the same fold pattern geometry. We believe that our compiled result proffers a library and guidelines for choosing compliant mechanisms for the creases of origami mechanical metamaterials.

Origami, Crease pattern, Compliant mechanism, Metamaterial, Gaussian process regression

Citation: Y. Miyazawa, H. Yasuda, and J. Yang, Design of compliant mechanisms for origami metamaterials, Acta Mech. Sin. **39**, 723169 (2023), https://doi.org/10.1007/s10409-023-23169-x

1. Introduction

In recent decades, the origami principle has been intensively studied to use origami as a building block of mechanical metamaterials. Origami-based structures have primarily gained attention from mathematicians and engineers, owing to their deployability for efficiently packing the planar or tubular structures, while offering precise control of how each section of structure deforms during deployment (e.g., solar panels [1, 2] and inflatable booms [3]). Later, their unconventional mechanical properties have increasingly gained attention [4]. To list a few exemplary properties, origami-inspired systems host load-bearing capability [5-7], variable stiffness [8-10], auxeticity [6, 11-13], and multistability [14-16], some of which are in-situ tunable. Moreover, the origami principle offers mechanics-based structural design, where we can determine the geometrical design of the origami based on the design space to obtain desired mechanical properties. As such, unlike conventional deployable systems, origami-based design allows predictable, yet complex geometrical morphing associated with unconventional mechanical properties of one's choice.

*Corresponding author. E-mail address: jkyang11@snu.ac.kr (Jinkyu Yang)
Executive Editor: Gengkai Hu

In general, origami-based structures are made from a sheet of materials where the crease deformation dominates the entire folding motion, while the facets remain undeformed or experience minimum distortion. To achieve such behavior, the facets and creases need to be clearly distinguished by their relative stiffness (i.e., facets being stiffer than creases). This suggests the vital role and contribution of choice and design of creases in origami behavior.

However, while innumerable origami patterns have been proposed and investigated, the significance of the compliant mechanism has been overlooked in the previous studies, except for a few attempts to directly study the compliant hinge [17-21]. These attempts include different designs of hinges, such as simple bending of soft material [20], etched or grooved hinge [17, 19, 21], stitched perforation [21], and complex so-called lamina-emergent mecahnism [17, 18]. The first three mechanisms rely heavily on the mechanical properties of the hinge material, which limits the controllability of the crease stiffness and could potentially suffer from failure due to material fatigue after repeated folding. In Ref. [17], various types of compliant hinges are presented, which mainly operate within the elastic deformation regime of the hinge material. Most of these hinges are based on lamina emergent mechanisms [22], which is a rather complex mechanism consisting of polygonal holes and multiple thin ligaments. Similarly, Ref. [18] proposed a compliant joint with in-situ variable stiffness and estimated the equivalent torsion spring constant of the hinge mechanism. The complex geometry of compliant hinges allows more design flexibility, but such complexity also poses difficulty in fabrication and assembly. Consequently, these designs have not been widely adopted in prototyping and analyzing origami-based mechanical metamaterials. Moreover, the previous studies on compliant hinges focus on the characteristics of the hinges themselves, and do not consider how the hinges affect the overall behavior of origami structures, such as force-displacement profile, multi-stability, and bulk stiffness.

On the other hand, some of the commonly used hinge mechanisms for origami-based mechanical metamaterials are hardly analyzed. Only recently, it has been pointed out that the choice of compliant mechanisms can determine the structure's mechanical properties of the structure [23]. However, the previous studies only provide qualitative insights into the bulk response of non-rigid origami through experimental and numerical demonstration. The connection between crease design parameters and the behavior of the rigid origami structure, and further, to the origami model parameter, is yet to be revealed.

To fill such knowledge gap between the understanding of macroscopic and mesoscopic (i.e., crease-level) behaviors of the origami-based metamaterials, in the current paper, we attempt to both quantitatively and qualitatively explore the influence of the hinge mechanism properties onto the origami mechanical behavior. To this end, we first list a few common compliant mechanisms to be reviewed associated with some previous origami studies. Then we use one of the commonly used designs to show the influence of the parameter on the behavior of origami units. Specifically, we employ a single hinge crease structure and Kresling origami to investigate the crease parameter effect in rigid and non-rigid origami, by conducting uni-axial compression tests to obtain force-displacement curves. Here, we use the bar-hinge model consisting of axial and torsion spring elements to describe our origami unit, and quantitatively analyze the relationship between compliant design parameters and model parameters. Interestingly, we observe that the change in compliant design parameters is reflected differently in rigid and non-rigid origami. Moreover, such phenomenon differs by the crease design parameter; some parameter shows a similar effect, and some parameter shows very distinctive effect in rigid and nonrigid origami. We believe that our study offers insight into selecting the compliant mechanisms and their corresponding parameters.

The paper is structured as follows: In Sect. 2, we introduce and review some common methods to fold a sheet of material into an origami structure. We identify the suitable compliant design for folding origami-based metamaterials for analyzing their mechanical response, including rigid and non-rigid origami. We then examine the influence of selected crease parameters on the effective stiffness of the hinge using the single hinge structure in Sect. 3. Section 4 considers the effect of the hinge parameter on the non-rigid origami behavior. For both rigid and non-rigid origami, we use a data-driven approach to analyze the parametric study result and examine how (e.g., linearly or nonlinearly) compliant mechanism parameters affect the folding behavior. In Sect. 5, we show a few examples of drastically altering the force-displacement landscape, e.g., from monostable to bistable, or nonlinear to linear, only by changing the compliant crease design parameters, but using the same Kresling origami geometry. In Sect. 6, we conclude the paper and present some possible directions for further study.

2. Compliant mechanism designs

Here, we briefly review five commonly used crease design approaches to origami-based mechanical metamaterials and assess the current state of compliant mechanisms in these metamaterials. Generally, origami-based structures employ compliant hinge design with relatively simple geometry, the folding of which is based on simple bending or folding of

the material, etching or grooving, or perforation. The following sections provide examples of each type of compliant mechanism design, including their potential advantages and disadvantages. The scenarios in which they have been used are also discussed.

2.1 Simple fold

The simple fold method folds the creases according to the reference lines without any compliant mechanisms. This method is used in origami art and can be effective in fast-prototyping using paper or thin polymer sheets (e.g., see a single hinge in Fig. 1a).

The advantage of this method is that it is simple and does not require additional steps. However, it can cause fatigue and fracture after being folded a few times. This is because compliant creases typically involve large deformation and can cause plastic deformation (due to, e.g., a wide range of fold angle, thick material, extremely small radius of curvature about the crease, etc.) [24]. This can significantly limit the repeatability and precision of origami-based mechanical metamaterials. In Ref. [25], the folded prototype is used to show the geometry of Kresling origami, but not for, e.g., measuring static or dynamic response.

2.2 Half-cut

The half-cut approach removes half of the material along the crease lines (see Fig. 1b), which is controlled by a laser cutter engraving or etching [19, 21, 26]. This method is more accurate than the simple fold, but the creases are still bent in their plastic deformation regime. For this reason, the design is employed in one-time use scenario, as we see in Ref. [26], where the origami stent is fabricated with titanium/nickel shape memory alloy for one-time deployment inside the blood vessel (Fig. 1b(i)). If used repeatedly, cracks can develop from and along the creases, causing them to tear apart.

2.3 Single-stitch perforation (SSP)

As shown in Fig. 1c, the SSP cuts out the holes (circular, oval, rectangular, line slit, etc.) along the creaselines [11, 21, 27-31] to reduce the material. This allows one to physically distinguish the rigid facet regions from compliant crease regions by relying on thin bridges (e.g., red circle in Fig. 1c). (The estimate of the effective torsion stiffness can be found in Ref. [17].) This improves fabrication accuracy over the simple fold approach. In most previous studies, the SSP approach is used for both proof-of-concept prototyping [28, 29] and measuring mechanical responses of the origami

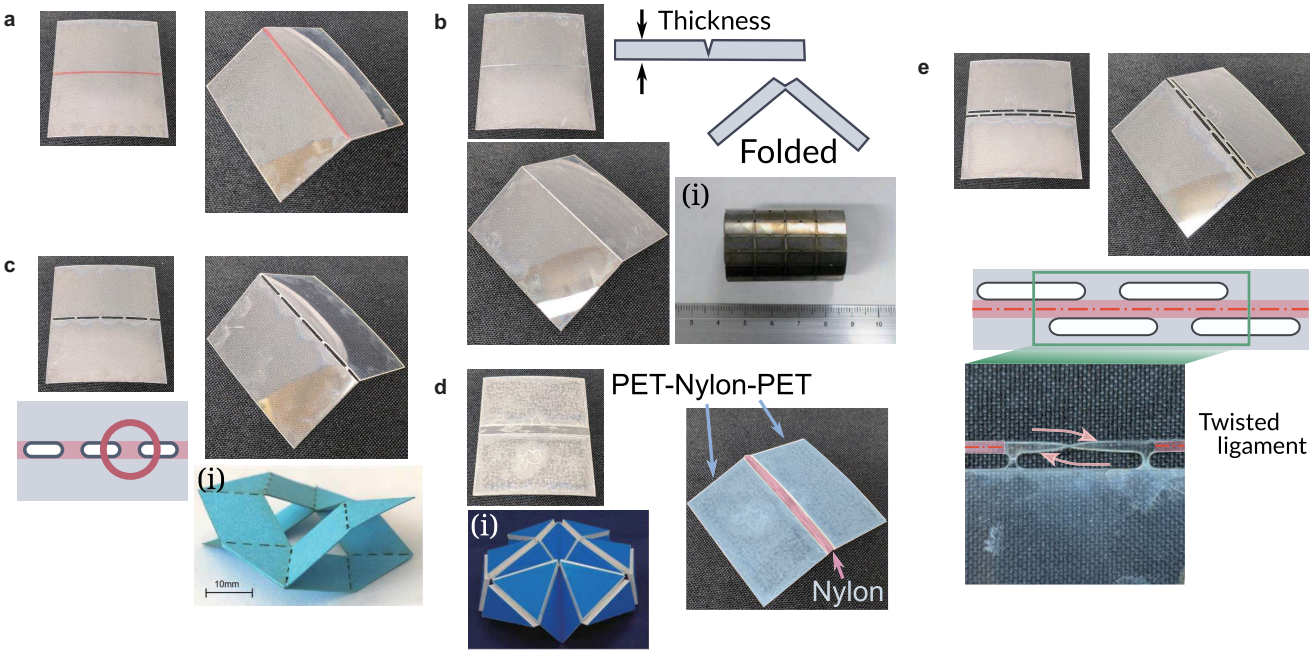

Figure 1 Various types of crease designs with samples made of PET sheet. **a** Simple-fold. Crease line marked with red marker pen for better visibility. **b** Half-cut. A thin white line in the top-left panel is engraved with the laser cutter. Sub-panel (i) shows an origami stent with etched crease lines [26]. **c** SSP. The stress concentration area is denoted by the red-shaded area. Sub-panel (i) shows a lockable origami unit with perforated creases [27]. **d** Multi-layered design. Single hinge prototype shows PET-based and nylon layers denoted as blue- and red-shaded regions. Sub-panel (i) shows a triangular Resch origami made of a thick panel and thin hinge material [32]. **e** Double-stitch perforation. Ligament twisting is shown in the magnified view on the bottom half of the panel. Sub-panel (i) in panel **b** is adapted with permission from Ref. [26], Elsevier. Sub-panel (i) in panel **c** is adapted with permission from Ref. [27], Springer Nature. Sub-panel (i) in panel **d** is adapted with permission from Ref. [32], Elsevier.

structures [27, 30, 31]. However, it still requires the plastic deformation (bending) of the material around the area indicated by the red shaded region in Fig. 1c, therefore does not fully resolve the vulnerability to fatigue and fracture that are present in the above two approaches.

2.4 Multi-layered

The methods above use a single layer of material with compliant creases, which can cause plastic deformation. To address this, multi-layered design distinguishes facets and creases by material type and thickness [19, 32, 33]. Figure 1d shows the schematics of the multi-layer (multi-material) method, made of polyethylene terephthalate (PET) layers and nylon layer, which play the role of stiff facets and compliant hinges, respectively. Reference [32] (see Fig. 1d(i)) fabricated Resch-patterned origami with thick panels and thin sheets for facets and creases, respectively. Similarly, Ref. [33] used cardboard paper (facet) and nylon sheets (crease) to fabricate leaf-like origami. The multi-layer approach, using different materials for the facets and creases, limits plastic deformation and improves folding accuracy and precision. In the above previous studies, the method was employed to capture the mechanical response of the origami structure, both in static and dynamic scenarios. However, this method is not suitable for complex origami designs due to its relatively involved fabrication process.

2.5 Double-stitch perforation (DSP)

The DSP is a modification to the SSP that limits plastic deformation and improves folding accuracy and precision. The discorectangular holes are made both on the left and right of the creaselines in an alternating order (see Fig. 1e). Such geometry allows the ligament to twist (see the bottom half of Fig. 1e), which typically resides within the elastic deformation regime, improving the resistance to fatigue and fracture.

The DSP crease design is often used for capturing the static and dynamic response rather than a proof-of-concept fast-prototyping [10, 23, 34]. Furthermore, unlike the other compliant mechanisms, the DSP crease is capable of hosting non-rigid origami motion, where the panel is intrinsically designed to bend or allow shear and twist along creases. Additionally, the DSP hinge offers another dimension of tunable parameters, changing the folding behavior of a hinge and panel deformation, which in turn drastically alters the behavior of the origami itself in a unique manner. The following sections show a few selected examples of origami behavior tuning using DSP.

3. Rigid origami with DSP crease

3.1 Physical setup and model

Here, we explore the effect of crease design parameters on the mechanical behavior of the origami structure by investigating the response of a single hinge unit. The DSP crease design parameters are as defined in Fig. 2a. In this study, we particularly investigate the relationship between the mechanical response and the parameters L and W, which are the length of the perforation and with spacing between the adjacent perforation, respectively. We note in passing that the length parameters B and H are also important parameters of the DSP hinge, but we limit our discussion to L and W in the current paper to cover broader examples of the crease parameter effect.

The single hinge unit consists of two panels connected through the compliant mechanism (in the current case, DSP crease hinge), and its geometrical parameters and variables are defined as in Fig. 2b. We assume two panels remain flat and rigid (i.e., area and side length remain constant), such that the hinge rotates about the segment $\overline{BB'}$, along which the torsion spring is embedded. Under the external load F along the z direction, the force-displacement relationship can be described as

$$F = \frac{4k_\theta w}{\sqrt{4l^2 - h^2}} \left[\sin^{-1}\left(\frac{h_0}{2l}\right) - \sin^{-1}\left(\frac{h}{2l}\right) \right], \tag{1}$$

where k_θ is the torsion spring coefficient per unit length, w is the width of the crease hinge, l is the length of the individual panel, h_0 is the initial height of the hinge unit, and $h = h_0 - u$ is the instantaneous height of the hinge unit.

3.2 Uni-axial compression test and data-driven modelling

In Fig. 2c, we show the experimental setup of the DSP hinge uni-axial compression test. The hinge is folded at its natural folding angle and mounted to the in-house load frame, where the displacement is controlled by a linear stage (Velmex, Inc. Bislide motorized linear stage MN10), and force is measured through the load cell (Kyowa Compact Tension/Compression Load Cell LUX-B-50N-ID). We fabricate the testing samples made of a 0.254 mm thick PET sheet, cut with a laser cutting machine (Universal Laser Systems, Inc. VLS4.60). For the parametric study, we fabricate the prototypes with the following ten parameter sets: L = (4, 6, 8, 10, 12) mm with B = 0.8, H = 0.7, and W = 0.8 mm kept constant; W = (0.4, 0.6, 0.8, 1.0, 1.2) mm with L = 10, B = 0.8, and H = 0.7 mm kept constant.

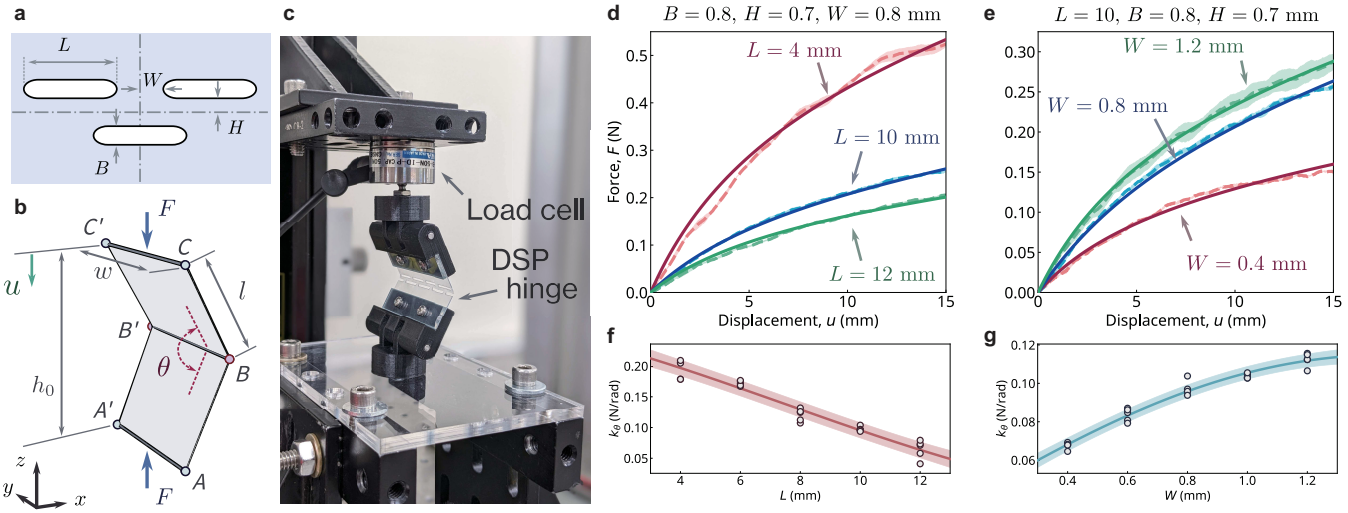

Figure 2 Relationships between spring coefficients and DSP crease parameters for single hinge unit. **a** Definition of the DSP crease parameters L, B, H, and W. **b** Schematical illustration of single hinge unit and definition of variables and parameters. **c** Experimental setup of the single hinge uni-axial compression test. **d** Force-displacement relationship with different values of DSP parameter L. Red, L = 4 mm; blue, L = 10 mm; green, L = 12 mm. Solid lines, model; dashed lines, experimental result. **e** Force-displacement relationship with different values of DSP parameter W. Red, W = 0.4 mm; blue, W = 0.8 mm; green, W = 1.2 mm. Solid lines, model; dashed lines, experimental result. Torsional spring coefficient k_θ as a function of length **f** L, and **g** W. Solid lines, prediction based on Gaussian process regression; shaded regions, standard deviation; open circle symbols, experimental data. Experimental data are obtained from five prototypes for each value of L and W.

Figure 2d and e shows the force-displacement curves of the three select cases, each for varying L and W cases, respectively. The dashed lines with shaded regions represent the experimental results, and the solid lines are drawn based on Eq. (1). Here, the torsion spring coefficient k_θ of the analytical model is estimated using the least-square method to fit the analytical profile to the experimental result. In general, we see the strain-softening behavior for any choice of the DSP parameter. For varying L case, the magnitude of the force amplifies as L decreases (negatively correlated). On the contrary, the varying W case shows the increase in magnitude as W increases (positively correlated).

To examine such correlation in detail, we show the spring coefficient k_θ as a function of length parameter L and W in Fig. 2f and g. Here, we use the Gaussian process regression to capture the variation of spring coefficients with respect to DSP parameters. The reason behind using the Gaussian process regression instead of conventional regression, e.g., linear regression, is to capture the behavior that is not necessarily linear. Especially, origami-based mechanical units are known to behave inherently nonlinear due to their complex geometrical configuration. In this study, we employ the Gaussian process regression function provided in the Python-based machine learning package, Scikit-learn [35]. We employ the combined kernel based on the radial basis function (RBF), which is one of the most commonly used kernels [36]. In combination, we use a constant kernel (CK) to scale the RBF, and a white noise kernel (WNK) to describe unknown noise, such that we obtain the kernel function: CK×RBF+WNK. During the regression by Scikit-learn GaussianProcessRegressor, the hyperparameter optimization is performed by restarting the optimizer ten times (i.e., the parameter `n_restarts_optimizer`=10). All other parameters follow the default values of GaussianProcessRegressor class, RBF, and ConstantKernel kernels [35].

Clearly, we see that the spring coefficients are negatively correlated to the length L. In particular, k_θ decreases linearly with L. On the contrary, as suggested by the magnitude of the force in Fig. 2e, the spring coefficients show a positive correlation for varying W case. Interestingly, unlike the linear correlation of varying L case, the spring coefficient is nonlinearly correlated to W, showing the saturating behavior as W increases. We believe that such positive and negative correlations between DSP parameters and the torsional stiffness of the hinge can be explained by the length of the twisted ligament. In general, the larger the L, the longer the twisted ligament. Similarly, the larger the W, the shorter the effective length of the twisted ligament. By preserving more material between perforations, the effective length of the ligament decreases (ligament length can be approximated as $\frac{L}{2} - W$). If we approximate the ligament as a rectangular cross-section beam under torsion, generally, the longer beam requires less torque to twist at a certain angle (i.e., torque, thus the torsional spring coefficient, is inversely proportional to the length of the beam). Here, we note in passing that Gaussian process regression reveals the notably nonlinear relationship between spacing W and k_θ while k_θ varies almost linearly with respect to length L.

4. Non-rigid origami with DSP crease

Given the contribution of the crease parameter to the mechanical response of the rigid origami (i.e., crease hinge), in this section, we examine the contribution of the DSP crease parameter in the non-rigid deformation of origami. As an example of non-rigid origami, here, we consider the Kresling origami unit [37] shown in Fig. 3a. The Kresling origami is one of the non-rigid origami structures, the folding behavior of which involves not only the crease folding but also facet deformation. We employ a DSP crease design to fabricate the Kresling prototypes (see Fig. 3a). The sample is made of a 0.254 mm thick PET sheet, folded after being cut out with a laser cutting machine (Universal Laser Systems, Inc. VLS4.60). The top and bottom surfaces are capped with 1.5 mm acrylic plates to ensure that all vertices stay on the same plane while the Kresling unit folds.

4.1 Physical setup and model

We use the geometrical and kinematic parameters shown in Fig. 3b to describe the Kresling origami unit. The unit cell has two coupled degrees of freedom: translation along z-axis (u) and rotation about z-axis (φ). As the unit cell gets compressed (u increases), the top surface rotates (φ varies) relative to the bottom surface, therefore exhibiting coupled behavior. The resultant force-displacement relationship under pure axial compression (i.e., no external torque applied) in the experiment is shown in Fig. 3c, denoted as a red dashed line.

To model this coupled folding behavior, we employ a truss model [38] by replacing the creases along segments $\overline{AC}$ and $\overline{BC}$ (denoted by red and blue solid lines in Fig. 3b) with linear spring elements, and segment $\overline{AB}$ (green solid line in Fig. 3b) with a linear torsion spring. The model gives the total potential energy expressed as

$$\Pi = \frac{N_\mathrm{p}}{2}\left[k_\mathrm{a}(a-a_0)^2 + k_\mathrm{b}(b-b_0)^2 + 2k_\psi(\psi-\psi_0)^2\right] - Fu - T\varphi, \tag{2}$$

where N_p is the number of vertices of the polygonal cross-section (for the case of Fig. 3, $N_\mathrm{p} = 6$), k_a and k_b are the linear axial spring coefficients of the axial spring elements along $\overline{AC}$ and $\overline{BC}$ respectively, and k_ψ is the torsion spring coefficient of the element along $\overline{AB}$. Variables a and b are the lengths of the element $\overline{AC}$ and $\overline{BC}$, and ψ is the angle between the horizontal surface and the triangular facet (e.g., $\triangle ABC$), which are a function of u and φ (see Ref. [34] for the explicit expression). The subscript 0 denotes the initial values. F is the axial force along z-axis, and T is the torque about z-axis.

Here, the truss model assumes the following relationship between k_b and k_a:

$$k_\mathrm{b} = \frac{a_0}{b_0}k_\mathrm{a}, \tag{3}$$

based on the linear bar element stiffness, $k = \frac{EA}{l}$, where k is the linear truss stiffness, E is the Young's modulus, A is the cross-sectional area, and l is the length of the truss bar element. By assuming that the material property (i.e., EA) does not change between element a and b, we obtain $EA = k_\mathrm{a}a_0 = k_\mathrm{b}b_0$, yielding Eq. (3).

By applying the principle of minimum potential energy, we obtain F and T as a function of u and φ (see Ref. [34] for the detail of derivation). This analytical force-displacement relationship is shown in Fig. 3c, denoted as a blue solid line. The experimental result is denoted as a red dashed line with a shaded region representing the standard deviation from three prototypes. Here, the spring coefficients are empirically determined using the least-square method to fit the model curve with the experimental curve obtained from a pure axial compression test (i.e., zero external torque T). As a result, we

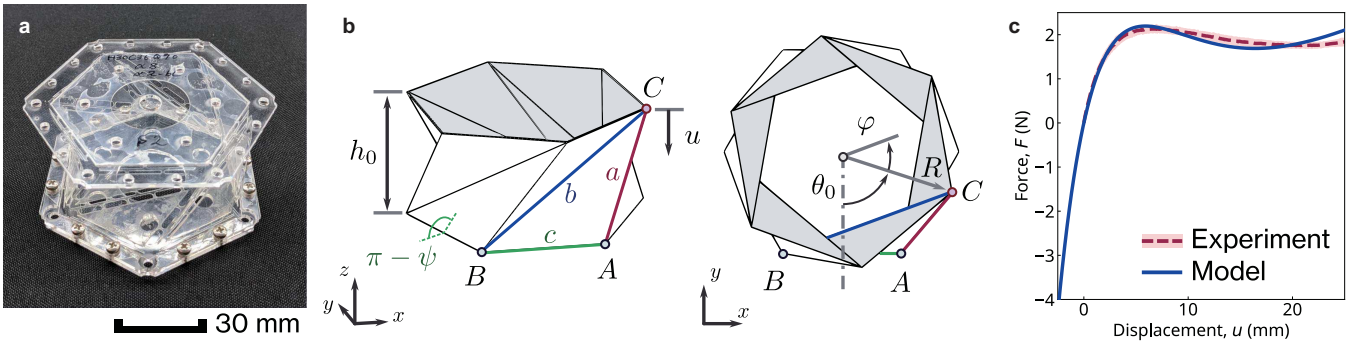

Figure 3 Geometrical parameter definition of Kresling origami. **a** Prototype made of PET sheet of thickness 0.254 mm. **b** Geometrical parameters and variables of Kresling origami. **c** Force-displacement profile. Blue solid line, truss-hinge model; red dashed line, averaged experimental result; red shaded region, standard deviation. Geometrical parameters used for panels **a** and **c** are: $h_0 = 30$ mm, $\theta_0 = 70°$, $R = 36$ mm.

can see the model agrees well with the experimental force-displacement profile. The spring coefficients are estimated to be $k_a = 1.211 \times 10^4$ N/m, $k_b = 7.486 \times 10^3$ N/m, and $k_\psi = 1.455 \times 10^{-2}$ N m/rad. (Note again that k_a and k_b are effective axial spring coefficients and k_ψ is the effective torsional spring coefficients that best describes the panel deformation and crease folding, respectively.)

4.2 Parametric study

Now, we examine the relationship between the Kresling origami stiffness (i.e., spring coefficients) and the size of the DSP discorectangular holes. The geometrical parameter of the Kresling prototype in this section is kept to $h_0 = 35$ mm, $\theta_0 = 70°$, and $R = 36$ mm. It has previously been suggested that the perforation size significantly affects both the qualitative behavior of the Kresling origami [23]. Here, we investigate the DSP parameter effect in a quantitative manner, by estimating the effective spring coefficient of the commonly used bar-and-hinge model of non-rigid origami. To this end, we again vary L and W of the DSP crease parameter (see Fig. 2a for definition), to study the Kresling origami behavior parametrically.

Figure 4a and b shows the selected force-displacement profiles for varying L and W cases, respectively. Similar to the single hinge constitutive relationship, we can see that the magnitude of the force decreases (increases) with an increase in length parameter L (W). For instance, we can see that the maximum force for the shorter $L = 4$ mm sample is about three times larger than, the longer $L = 12$ mm sample. Such variation can qualitatively be seen in the spring coefficients as well. While the $L = 12$ mm sample estimates the spring coefficients to be $k_a = 2.595 \times 10^4$ N/m and $k_\psi = 0.0536$ N m/rad, the $L = 4$ mm sample coefficients are $k_a = 6.585 \times 10^4$ N/m and $k_\psi = 0.1849$ N m/rad. Note that the axial and torsional spring coefficients of the shorter L sample are 2.5 times and 3.5 times larger than the longer L sample, respectively.

We show the spring coefficients k_a and k_ψ as a function of length parameter L in Fig. 4c. We plot $L = 4$ and 12 mm results and two additional data sets for $L = 6$, $L = 8$, and $L = 10$ mm, with $B = 0.8$, $H = 0.7$, $W = 0.8$ mm, denoted as open circle symbols. Similar to the hinge study in the previous section, the solid lines with shaded regions represent the prediction by Gaussian process regression with standard deviation. Clearly, we see that the spring coefficients are negatively correlated to the length L. Moreover, both k_a and k_ψ show linear correlation with respect to L, which agrees well with the rigid origami hinge parametric study. Note that the magnitude of k_ψ matches with that of a single hinge structure for all values of L, which suggests the validity of the estimated values of the Kresling model.

Figure 4d shows the axial and torsional spring coefficients as a function of parameter W in sub-panel (i) and (ii), respectively. Here, we fabricate prototypes with five different parameter sets: $W = (0.4, 0.6, 0.8, 1.0, 1.2)$ mm with $L = 10$, $B = 0.8$, $H = 0.7$ mm. At a glance, we see that the order of magnitude of the spring element stiffness resides within a similar range for rigid and non-rigid origami cases. However, interestingly, varying W case shows different trend than in the single hinge case. While the single hinge parametric study shows the decreasing slope of the prediction curve, the Kresling origami case shows the increasing slope of the prediction curve. This suggests that the parameter W contributes predominantly to the facet deformation of the non-rigid origami, and vice versa, which is contrary to the effect of length L. We believe that this discrepancy between the rigid and non-rigid origami case can bring insight into improving the conventional origami models (e.g., bar-hinge model), by taking crease geometry and parameters into account.

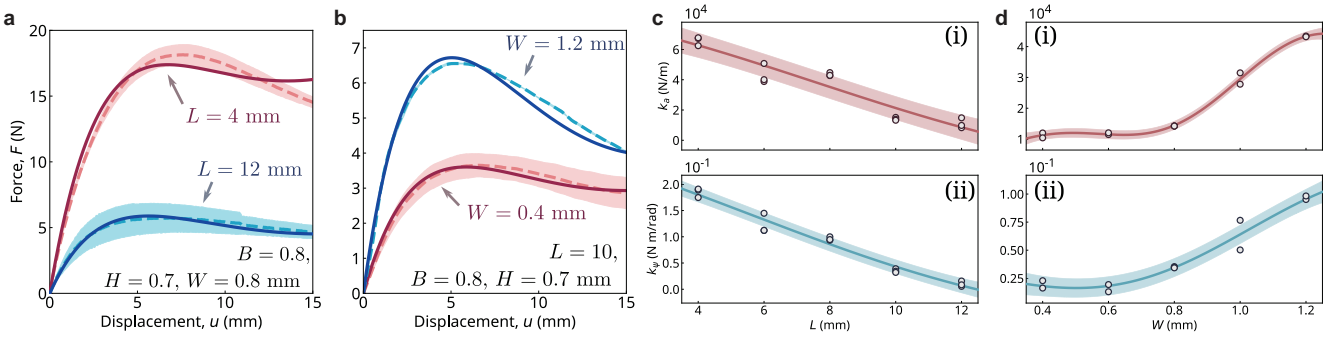

Figure 4 Kresling origami static response and DSP parameters. **a** Force-displacement relationship of different values of L. Red, $L = 4$ mm; blue, $L = 12$ mm. **b** Force-displacement relationship of different values of W. Red, $W = 0.4$ mm; blue, $W = 1.2$ mm. Solid lines, model; dashed lines, experimental result. Axial spring coefficient k_a and torsional spring coefficient k_ψ as a function of **c** length L, and **d** length W. Red, axial spring coefficients k_a; blue, torsional spring coefficients k_ψ. Solid lines, prediction based on Gaussian process regression; shaded regions, standard deviation; open circle symbols, experimental data. Experimental data are obtained from three prototypes for each value of L, and two prototypes for each value of W.

5. Reconfiguration of constitutive relation landscape

The previous section shows that the change in crease parameters can significantly affect the spring coefficients k_a, k_b, and k_ψ while preserving the landscape of the force-displacement curve to be strain-softening and monostable. Here, we show that the combination of such stiffness change, in turn, can even alter the overall landscape of the force-displacement curve by exploring two examples.

In Fig. 5a, we show the force-displacement relationships of the Kresling origami with $h_0 = 50$ mm, $\theta_0 = 70°$, and $R = 36$ mm, made of PET sheet using different DSP parameter sets. Unlike the prototype in the previous section ($h_0 = 35$ mm, $\theta_0 = 70°$, and $R = 36$ mm), the force-displacement curve now shows a significant decrease in the force after reaching the peak, which is especially prominent with DSP parameter set (L, B, H, W) = (4, 0.8, 0.7, 0.8) mm, where the maximum force $F \approx 16$ N is reached around $u \approx 6$ mm, as shown by the red solid line labeled as A-I in Fig. 5a. The minimum force reads about half of the maximum force, then rapidly recovers above the peak force. Such force-displacement landscape is very typical for the system with snap-through under force-controlled loading conditions, while having only one stable fixed point (i.e., monostable).

Following the regression result we saw in the previous section, we find that by increasing L from 4 mm to 12 mm (blue solid line labeled as A-II in Fig. 5a), the overall magnitude of the force drops significantly (i.e., the maximum force differs by a factor of 4). In both cases, the local minimum around $u = 18$ mm is still positive (i.e., compressive force), the unit of which hosts only one stable energy state at $u = 0$ (i.e., monostable), as suggested by the potential energy curve in Fig. 5a(i). Interestingly, if we tailor the DSP parameters by combining two different DSP parameter sets for each type of spring, the minimum force becomes negative (i.e., tensile force). In the current study, we assign (L, B, H, W) = (10, 1.0, 0.4, 0.4) to creases along segement with lengths a and b, and (L, B, H, W) = (4, 1.0, 0.4, 0.6) to creases along segment with length c (see inset of Fig. 5a or Fig. 3b). The Kresling unit hosts two stable energy states (i.e., bistable), at $u = 0$ and $u \approx 22$ mm. As such, the unit cell can be designed to be multi-stable by selecting and combining the DSP parameter.

Now, we show another example of the rich versatility of the DSP crease parameter choice, by fabricating Kresling origami with geometrical parameter $h_0 = 35$ mm, $\theta_0 = 90°$, and $R = 36$ mm, made of a paper sheet (3-ply Strathmore 500 Series Bristol). Figure 5b shows the force-displacement curves from four different DSP parameter sets: Set B-I, (L, B, H, W) = (10.1, 0.5, 0.5, 0.95); Set B-II, a hybrid of (10.6, 1.0, 0.5, 0.7) and (6.6, 1.0, 0.5, 0.7); Set B-III, (14, 1.0, 0.5, 0.7); Set B-IV, (10.6, 1.0, 0.3, 0.7), with units in mm. First, if we examine Set I, the profile is very similar to that of Fig. 5a, where the unit cell hosts snap-through behavior when it reaches the local maximum. However, if we slightly change to DSP parameter to Set II, the dip disappears, such that the force monotonically increases while going through the near-zero stiffness regime from $x \approx 5$ to $x \approx 8$ mm.

While the example in Fig. 5a preserves structural instability by having a snap-through profile regardless of parameter choice, we see that such instability is completely removed in the example shown in Fig. 5b. Moreover, if we further change the DSP parameter to Set B-III, where L is much larger, we see a long-lasting plateau region starting from $u \approx 5$ mm after a slight increase of the force in a linear manner. In Set B-IV, we have the perforation length L and the ligament width H being smaller than in Set B-III. Interestingly enough, the nearly zero-stiffness region in Set B-III is now replaced

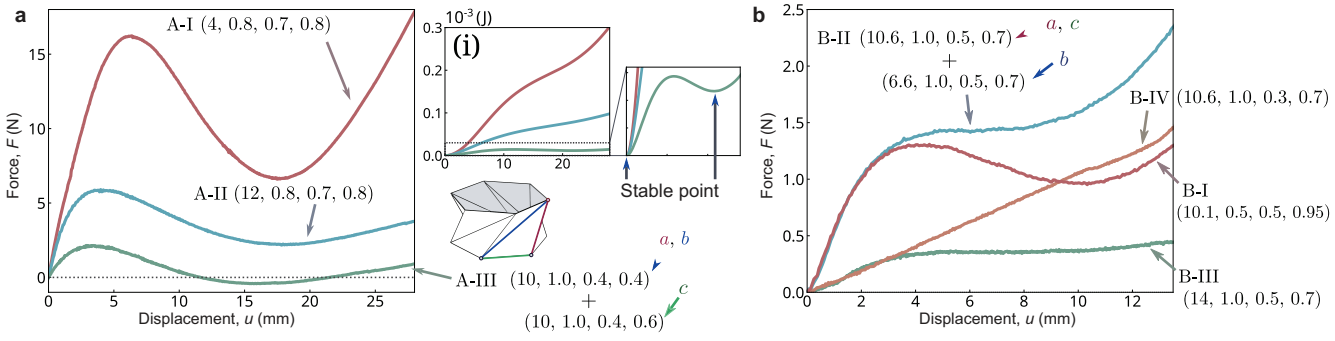

Figure 5 Force-displacement landscape with different DSP crease parameters. **a** Force-displacement relationships of the Kresling prototype with $h_0 = 50$ mm, $\theta_0 = 70°$, and $R = 36$ mm, made of PET sheet. Sub-panel (i) shows the potential energy obtained by numerically integrating the corresponding force-displacement curves with Simpson's rule. Red solids lines, parameter set A-I; blue, A-II; green, A-III. **b** Force-displacement relationships of the Kresling prototype with $h_0 = 35$ mm, $\theta_0 = 90°$, and $R = 36$ mm, made of Bristol art paper. Red solids lines, parameter set B-I; blue, B-II; green, B-III; orange, B-IV. DSP parameters are ordered as (L, B, H, W) with the unit in mm.

by linearly increasing behavior. Note that such drastic tunability, ranging from linear to nonlinear force-displacement landscape, is achieved only by changing the DSP parameter, keeping the bulk geometry of the Kresling origami consistent. This clearly suggests the significance of compliant mechanism design in origami-based metamaterials, which provides additional dimensions of tuning parameters.

6. Conclusion

In conclusion, we have reviewed and examined the compliant mechanism design for the origami mechanical metamaterials. Some of the exemplary compliant mechanisms include simple fold, half-cut (or etching), SSP and DSP, and multi-layered crease, each of which offers unique benefits, for instance, fast-prototyping, folding accuracy and precision, or tolerance in fatigue. Out of five common designs, we select DSP crease design to be further examined. Specifically, the DSP parameters (e.g., perforation size) have been investigated from an origami modeling standpoint, for both rigid and non-rigid origami structures. We conduct the uni-axial compression test on the single hinge and Kresling origami units fabricated using different sets of DSP parameters. We then feed the experimental force-displacement relationship into the analytical models based on torsion spring elements for rigid origami, and axial and torsion spring elements for non-rigid origami to estimate the stiffness of the origami units. The extracted spring coefficients are plotted against length parameters L and W, the relationships of which were described using Gaussian process regression.

The data-driven regression revealed the unique contribution of DSP parameters to the spring stiffness, which differs for rigid and non-rigid origami. Specifically, while the change of length parameter L contributed to origami stiffness in a likewise manner regardless of the rigid or non-rigid nature of origami, the change in W acted on the stiffness differently. Lastly, we showed a few examples of changing the overall mechanical response of the Kresling origami by only changing DSP parameters. Here, we report that we can easily tune the Kresling unit cell to be monostable or bistable, and the force-displacement curve to be linear or nonlinear. We envision that these findings shall not only proffer insight into selecting and designing compliant mechanisms for origami-based mechanical metamaterials, but also hints at extending the versatility of origami systems based on a data-driven approach.

Author contributions ***Yasuhiro Miyazawa:*** *Conceptualization, Data curation, Formal analysis, Investigation, Methodology, Resources, Software, Validation, Visualization, Writing – original draft, Writing – review & editing.* ***Hiromi Yasuda:*** *Conceptualization, Writing – review & editing.* ***Jinkyu Yang:*** *Conceptualization, Resources, Writing – review & editing, Supervision, Project administration, Funding acquisition.*

Acknowledgements *Yasuhiro Miyazawa and Jinkyu Yang are grateful for the support from the U.S. National Science Foundation (Grant Nos. 1933729 and 2201612) and Toyota Research Institute North America (TEMA). Jinkyu Yang acknowledges the support from SNU-IAMD, SNU-IOER, and National Research Foundation grants funded by the Korea government (Grant Nos. 2023R1A2C2003705 and 2022H1D3A2A03096579 (Brain Pool Plus by the Ministry of Science and ICT)).*

1 Koryo Miura, Method of packaging and deployment of large membranes in space, Technical Report (The Institute of Space and Astronautical Science, Sagamihara, Kanagawa, 1985).
2 S. A. Zirbel, R. J. Lang, M. W. Thomson, D. A. Sigel, P. E. Walkemeyer, B. P. Trease, S. P. Magleby, and L. L. Howell, Accommodating thickness in origami-based deployable arrays, J. Mech. Des. Transact. ASME, **135**, (2013).
3 M. Schenk, A. D. Viquerat, K. A. Seffen, and S. D. Guest, Review of inflatable booms for deployable space structures: Packing and rigidization, J. Spacecraft Rockets **51**, 762 (2014).
4 S. Li, H. Fang, S. Sadeghi, P. Bhovad, and K. W. Wang, Architected origami materials: How folding creates sophisticated mechanical properties, Adv. Mater. **31**, 1805282 (2019).
5 Y. Yoshimaru, On the mechanism of buckling of a circular cylindrical shell under axial compression, Technical Report (National Advisory Committee for Aeronautics, Washington, 1955).
6 H. Yasuda, and J. Yang, Reentrant origami-based metamaterials with negative Poisson's ratio and bistability, Phys. Rev. Lett. **114**, 185502 (2015).
7 M. Schenk, and S. D. Guest, Geometry of Miura-folded metamaterials, Proc. Natl. Acad. Sci. USA **110**, 3276 (2013).
8 H. Fang, S. C. A. Chu, Y. Xia, and K. W. Wang, Programmable self-locking origami mechanical metamaterials, Adv. Mater. **30**, 1706311 (2018).
9 T. Mukhopadhyay, J. Ma, H. Feng, D. Hou, J. M. Gattas, Y. Chen, and Z. You, Programmable stiffness and shape modulation in origami materials: Emergence of a distant actuation feature, Appl. Mater. Today **19**, 100537 (2020).
10 Y. Miyazawa, H. Yasuda, H. Kim, J. H. Lynch, K. Tsujikawa, T. Kunimine, J. R. Raney, and J. Yang, Heterogeneous origami-architected materials with variable stiffness, Commun. Mater. **2**, 110 (2021).
11 S. Kamrava, D. Mousanezhad, H. Ebrahimi, R. Ghosh, and A. Vaziri, Origami-based cellular metamaterial with auxetic, bistable, and self-locking properties, Sci. Rep. **7**, 46046 (2017).
12 Y. Tang, and J. Yin, Design of cut unit geometry in hierarchical kirigami-based auxetic metamaterials for high stretchability and compressibility, Extreme Mech. Lett. **12**, 77 (2017).
13 A. Benouhiba, P. Rougeot, N. Andreff, K. Rabenorosoa, and M. Ouisse, Origami-based auxetic tunable Helmholtz resonator for noise control, Smart Mater. Struct. , 035029 (2021).
14 J. L. Silverberg, A. A. Evans, L. McLeod, R. C. Hayward, T. Hull, C. D. Santangelo, and I. Cohen, Using origami design principles to fold reprogrammable mechanical metamaterials, Science **345**, 647 (2014).
15 H. Yasuda, T. Tachi, M. Lee, and J. Yang, Origami-based tunable truss structures for non-volatile mechanical memory operation, Nat. Commun. **8**, 962 (2017), arXiv: 1702.05402.
16 J. E. Suh, Y. Miyazawa, J. Yang, and J. H. Han, Self-reconfiguring and stiffening origami tube, Adv. Eng. Mater. **24**, 2101202 (2022).
17 I. L. Delimont, S. P. Magleby, and L. L. Howell, Evaluating compliant hinge geometries for origami-inspired mechanisms, J. Mech. Robot. **7**, (2015).
18 Z. Xie, L. Qiu, and D. Yang, Design and analysis of a variable stiffness inside-deployed lamina emergent joint, Mech. Mach. Theor. **120**, 166 (2018).

19 M. A. Wagner, J. L. Huang, P. Okle, J. Paik, and R. Spolenak, Hinges for origami-inspired structures by multimaterial additive manufacturing, Mater. Des. **191**, 108643 (2020).
20 H. Zhang, H. Feng, J. L. Huang, and J. Paik, Generalized modeling of origami folding joints, Extreme Mech. Lett. **45**, 101213 (2021).
21 W. Ma, X. Liu, X. Qiu, Y. Zhou, Y. Liu, W. Fu, X. Guo, Z. Qian, K. Du, and J. Cai, Comparative folding/unfolding performance of notch-type compliant joints, Case Studies Construct. Mater. **18**, e01760 (2023).
22 J. O. Jacobsen, B. G. Winder, L. L. Howell, and S. P. Magleby, Lamina emergent mechanisms and their basic elements, J. Mech. Robot. **2**, (2010).
23 H. Y. Hwang, Effects of perforated crease line design on mechanical behaviors of origami structures, Int. J. Solids Struct. **230-231**, 111158 (2021).
24 H. Yasuda, T. Yein, T. Tachi, K. Miura, and M. Taya, Folding behaviour of Tachi-Miura polyhedron bellows, Proc. R. Soc. A **469**, 20130351 (2013).
25 N. Kidambi, and K. W. Wang, Dynamics of Kresling origami deployment, Phys. Rev. E **101**, 063003 (2020), arXiv: 2003.10411.
26 K. Kuribayashi, K. Tsuchiya, Z. You, D. Tomus, M. Umemoto, T. Ito, and M. Sasaki, Self-deployable origami stent grafts as a biomedical application of Ni-rich TiNi shape memory alloy foil, Mater. Sci. Eng.-A **419**, 131 (2006).
27 A. Jamalimehr, M. Mirzajanzadeh, A. Akbarzadeh, and D. Pasini, Rigidly flat-foldable class of lockable origami-inspired metamaterials with topological stiff states, Nat. Commun. **13**, 1816 (2022).
28 Dae-Young Lee, Ji-Suk Kim, Sa-Reum Kim, Je-Sung Koh, and Kyu-Jin Cho, The deformable wheel robot using magic-ball origami structure: Proceedings of the ASME 2013 International Design Engineering Technical Conferences and Computers and Information in Engineering Conference, Volume 6B: 37th Mechanisms and Robotics Conference, Portland, 2013.
29 T. Tachi, Designing freeform origami tessellations by generalizing Resch's patterns, J. Mech. Des. **135**, (2013).
30 S. Wu, Q. Ze, J. Dai, N. Udipi, G. H. Paulino, and R. Zhao, Stretchable origami robotic arm with omnidirectional bending and twisting, Proc. Natl. Acad. Sci. USA **118**, e2110023118 (2021).
31 Q. Zhang, H. Fang, J. Xu, and S. Li, Data-driven modeling of a pneumatic yoshimura-origami structure with tunable dynamics: Proceedings of ASME 2022 International Design Engineering Technical Conferences and Computers and Information in Engineering Conference, St. Louis, 2022.
32 F. Yang, M. Zhang, J. Ma, Z. You, Y. Yu, Y. Chen, and G. H. Paulino, Design of single degree-of-freedom triangular resch patterns with thick-panel origami, Mech. Mach. Theor. **169**, 104650 (2022).
33 H. Yasuda, K. Johnson, V. Arroyos, K. Yamaguchi, J. R. Raney, and J. Yang, Leaf-like origami with bistability for self-adaptive grasping motions, Soft Robot. **9**, 938 (2022).
34 Y. Miyazawa, C. W. Chen, R. Chaunsali, T. S. Gormley, G. Yin, G. Theocharis, and J. Yang, Topological state transfer in Kresling origami, Commun. Mater. **3**, 62 (2022), arXiv: 2202.01398.
35 F. Pedregosa, G. Varoquaux, A. Gramfort, V. Michel, B. Thirion, O. Grisel, M. Blondel, P. Prettenhofer, R. Weiss, V. Dubourg, J. Vanderplas, A. Passos, D. Cournapeau, M. Brucher, M. Perrot, and E. Duchesnay, Scikit-learn: Machine learning in Python, J. Mach. Learning Res. **12**, 2825 (2011).
36 C. E. Rasmussen, and C. K. I. Williams, Gaussian Processes for Machine Learning (The MIT Press, Cambridge, 2018).
37 B. Kresling, Origami-structures in nature: Lessons in designing "smart" materials, Mater. Res. Soc. Symp. Proc. **1420**, 42 (2012).
38 H. Yasuda, Y. Miyazawa, E. G. Charalampidis, C. Chong, P. G. Kevrekidis, and J. Yang, Origami-based impact mitigation via rarefaction solitary wave creation, Sci. Adv. **5**, eaau2835 (2019), arXiv: 1805.05909.

折纸超材料合规机制的设计

Yasuhiro Miyazawa, Hiromi Yasuda, Jinkyu Yang

摘要 折纸作为一种折纸艺术, 几个世纪以来一直被艺术家们广泛探索. 直到最近几十年, 它才因其复杂的几何形状和丰富的力学性能而受到数学家和工程师的关注. 以折纸为灵感的超材料的激增为材料和结构的设计打开了一扇新的窗口. 通常, 会根据标有合规机制的折痕线折叠一张材料来构建折纸结构. 尽管它们在折纸制造中很重要, 但在折纸超材料的设置中, 这种合规机制尚未得到探索. 本研究探讨了合规机制设计参数与折纸力学性能之间的关系. 尤其我们采用的是单铰链折痕和Kresling折纸, 这是刚性和非刚性折纸单元的代表性示例, 采用双针穿孔兼容机构设计制造. 我们使用不同的折痕参数进行轴向压缩测试, 并将结果拟合到由轴向和扭转弹簧组成的棒铰折纸模型中. 使用高斯回归过程提取弹簧系数和折痕参数之间的关系. 结果表明, 折痕参数的变化以非常不同的方式对每个弹簧元件有显著贡献, 这表明合规机制根据变形模式的微调性. 特别是, 刚性和非刚性折纸的弹簧刚度随折痕参数而变化不同, 即使调整了相同的折痕参数也是如此. 此外, 我们报道了Kresling折纸的定性静态响应只需改变折痕参数, 就可以在单稳态和双稳态之间, 或者线性和非线性之间调节, 同时可以保持相同的折叠图案几何形状. 我们相信, 我们的结果为折纸机械超材料的褶皱选择合规机制提供了一个库和指南.